Compact PIN-Diode-Based Silicon Modulator Using Side-Wall-Grating Waveguide

Suguru Akiyama, Masahiko Imai, Takeshi Baba, Takeshi Akagawa, Naoki Hirayama, Yoshiji Noguchi, Miyoshi Seki, Keiji Koshino, Munehiro Toyama, Tsuyoshi Horikawa, and Tatsuya Usuki, *Member, IEEE*

***Abstract*—We developed PIN-diode-based silicon Mach–Zehnder modulators, which have side-wall-gratings in the phase-shifter sections. Such passive waveguides with gratings were fabricated using ArF immersion lithography, which showed a small scattering loss of 0.4 dB/mm. We extensively investigated the forward-biased operation of the modulators by using equivalent circuit analysis and the measurement of the fabricated devices. We argue carrier recombination time only plays a minor role for the overall performance of the modulator. Dependences of the modulation efficiency on other various critical parameters are discussed. In particular, if we use relatively short phase shifter, the forward-biased operation provides smaller $V_\pi L$ than reversed one even at high frequency of 20 GHz, at the expense of the narrow bandwidth. Our approach enables high-speed operation up to 50 Gb/s, by using phase shifter as short as 250 μm and preemphasis signals. For 12.5-Gb/s operation, the modulator cell size was only 300 μm $\times$ 50 μm, which was suitable for the applications of high-density optical interconnects.**

***Index Terms*—Modulation, optoelectronics, photonic integrated circuits, waveguide modulators.**

I. Introduction

LARGE-scale integrated circuits (LSIs) based on silicon electronics currently exhibit an interconnect-bottleneck when further increasing computing ability, particularly in interchip transmissions [1]. Optical interconnects are one of candidates for solving this bottleneck problem due to its wide-bandwidth property. Various configurations have been proposed and demonstrated for the optical interconnects [1]–[5]. Silicon optical interposers (SOIPs) are one of such configurations, on which optical waveguides and optoelectronic devices are integrated at high density and LSIs are flip-chip bonded [5]. Such photonics-electronics convergent systems enable wide-bandwidth and high-density optical interconnect among LSIs, instead of conventional electrical ones. To achieve the desired transmission, an array of high-speed and compact silicon modulators is essential. A number of modulators should be placed in the limited space in the vicinity of the LSIs, while each modulator operates at as high speed as possible. In addition, low-driving voltage is required for the modulators so that complementary metal-oxide-semiconductor (CMOS) circuits can drive them.

Mach–Zehnder modulators (MZMs), which are based on the free-carrier plasma (FCP) effect in silicon, are suitable for SOIPs [6]–[25]. FCP is virtually only an electrooptic effect, which occurs in silicon [26], which makes these modulators a primary choice to ensure full compatibility with the conventional silicon fabrication process. In addition, the FCP effect is insensitive to wavelength and temperature, unlike other effects induced by change in the direct bandgap.

MZMs based on reverse-biased PN-diodes are most commonly investigated and are formed in rib-waveguides on silicon-on-insulator (SOI) substrate [11]–[18]. The waveguides have thin slab layers of silicon on both sides of the core. Although the thickness of the slab layers affects the performance of the modulator, its controllability only relies on the duration time in the silicon etching process. In addition, mode conversion is needed to connect these rib-waveguides with other photonic components such as wavelength MUX/DEMUX in SOIPs. For such passive components, wire-type waveguides without side slab layers are standard.

In MZM operation, reverse-biased diodes act as capacitor with relatively small capacitance (0.2−0.7 pF/mm) [16]–[18], which is suitable to obtain a wide-modulation bandwidth of tens of gigahertz in terms of the resistance-capacitance (RC) time constant. However, they provide only limited modulation efficiency per unit length because they can store a relatively small amount of charges for a given driving voltage. As a consequence, MZMs are usually as long as one or several millimeters and not small enough for SOIP applications. Although microring resonators can enhance the modulation efficiency, they approach the speed limit caused by the photon lifetime of the resonator. To increase capacitance, a high-doped junction is not tolerated both for MZMs and resonator-based modulators if the optical loss increases.

This paper presents our compact silicon modulators, which were developed for the SOIP applications [20]–[22]. The modulators have side-wall-grating waveguides in the phase shifter sections. The side-wall-grating structure is easy to fabricate in terms of repeatability of the etching process of waveguides because no thin slab layer has to remain. Since the critical dimension of such waveguide is as small as about 80 nm, all

Manuscript received March 1, 2013; revised June 17, 2013 and August 5, 2013; accepted August 9, 2013. Date of publication September 25, 2013; date of current version September 27, 2013. This work was supported by grant by JSPS through FIRST Program initiated by CSTP.

S. Akiyama, M. Imai, T. Baba, T. Akagawa, and T. Usuki are with the Photonics Electronics Technology Research Association (PETRA), Tsukuba, Ibaraki 305-8569 Japan (e-mail: s-akiyama@petra-jp.org; m-imai@petra-jp.org; t-baba@petra-jp.org; t-akagawa@petra-jp.org; t-usuki@petra-jp.org).

N. Hirayama, Y. Noguchi, M. Seki, K. Koshino, M. Toyama, and T. Horikawa are with the National Institute of Advanced Industrial Science and Technology (AIST), Tsukuba, Ibaraki 305-8569 Japan (e-mail: naoki.hirayama@aist.go.jp; yoshiji-noguchi@aist.go.jp; seki.miyoshi@aist.go.jp; koshino.keiji@aist.go.jp; munehiro.toyama@aist.go.jp; tsuyoshi.horikawa@aist.go.jp).

Color versions of one or more of the figures in this paper are available online at http://ieeexplore.ieee.org.

Digital Object Identifier 10.1109/JSTQE.2013.2278438

modulators in our works were fabricated by using electron-beam lithography [20]–[23]. In this paper, we present passive side-wall-grating waveguides, which were fabricated by photolithography using ArF immersion exposure, for the first time. The fabricated passive waveguides with side-wall-grating exhibited a scattering loss of less than 0.4 dB/mm.

A main topic of this paper is a detailed study on efficiency of silicon modulators based on forward-biased diodes [8]–[12], [19]–[25]. Using that operation modes, we have already achieved high-speed operation up to 50 Gb/s of MZMs by using phase shifters with side-wall gratings [20]–[22]. In those experiments, the modulators provide efficient modulation, and the phase shifters were as short as 250 μm. Although those works extended the potential of the forward-biased operation of the diodes, it remains unclear what quantity really limits the performance of them.

In this paper, we present our comprehensive study to understand the operation of modulators based on forward-biased diodes. We analyzed such operation using equivalent circuit models. The circuit model was essentially same as that proposed by Zhou [10]. We examined the model by applying the parameters obtained from the measured S-parameters. As a consequence, we found that carrier recombination time is not the only factor that determines frequency characteristics of the modulator, and it plays only a minor role for the overall performance of the modulators.

Based on those analyses, we experimentally evaluated the efficiency of the modulators. The bandwidth of forward-biased operation is usually several hundred megahertz [8]–[12], [19]–[23]. Therefore, these MZMs require driving circuits that can compensate frequency dependences of the modulator for broadband operation of tens of gigabit per second. Several methods were developed and demonstrated for such compensation including preemphasis signals [8], [9], [19]–[25], [27]. If these methods will be readily available in future systems, the efficiency of the modulator at the highest frequency component in signals will be more important than broadband characteristics. In this context, we measured the efficiencies of forward-biased operation of PN-diodes at different frequencies, and compared them with different bias-voltages, doping profiles, and the length of the phase shifters.

The forward-biased operation can provide high modulation efficiency even by a short phase shifter due to their large capacitance. For 250-μm long phase shifters, we obtained the similar results as reported by Spector *et al.* [11]; the efficiency of forward-biased operation is higher than those of reversed operation at frequencies up to 20 GHz. On top of that, our experimental results show that the forward-biased operation provides higher efficiency than the reversed one even at 20 GHz when we use the shorter, 100-μm long phase shifter.

Finally, we show the results of high-speed large-signal modulation experiments [20]–[22]. We achieved up to 50-Gb/s [22] operation of our fabricated MZMs with forward-biased diodes and preemphasis signals generated using a finite-impulse-response (FIR) filter. The high-efficiency of the forward-biased operation enabled the use of a phase shifter as short as 100–250-μm for SOIP applications. For 12.5-Gb/s operation, our new modulator cell pattern was used, which was only 300-μm wide and 50-μm high.

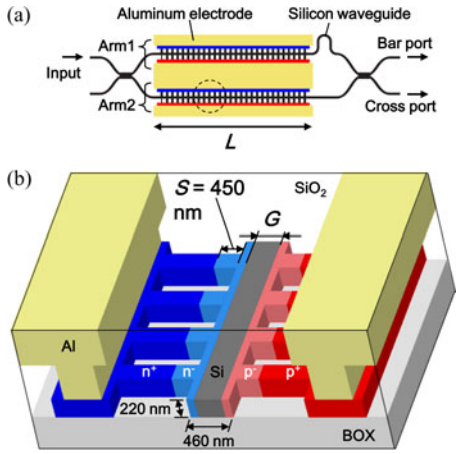

Fig. 1. Schematic view of MZM with side-wall-grating waveguides fabricated on SOI substrate. (a) Top view. (b) Close up of phase shifter.

II. Modulator With Side-Wall-Grating Waveguides

A. Device Structure

Fig. 1 is a schematic view of one of our modulators, which is basically the same as in our previous studies [20]–[22]. As shown in Fig. 1(a), a Mach–Zehnder interferometer (MZI) consists of silicon-based waveguides and two multimode interference (MMI) couplers on a SOI substrate. Fig. 1(b) shows a close-up of one of the two phase shifters of this MZM. On both sides of the waveguide core, the side-wall gratings were formed with periodically placed fins. These fins act as paths via which free carriers, such as electrons and holes, are injected into or extracted from the core during MZM operation. Our MZMs have a uniform thickness of silicon over the entire structure, unlike the conventional rib waveguide. In the etching process for defining the core, a buried oxide layer acts as a stopping layer; therefore, less controllability is required in the process than that for conventional rib-waveguides.

Design of the doping profile around the waveguide-core is critical for high-speed and efficient operation of forward-biased diodes, the same as those of reverse-biased diodes. The silicon pads and outer parts of the fins of the gratings were highly p- or n-type doped at 10^{20} cm^{-3}, denoted as p^+ and n^+ in Fig. 1(b). The distances between high-doped regions and the side-wall of the core are denoted as S and as small as 450 nm, which must be small to obtain efficient operation of the forward-biased modulators at high frequencies [21]. To obtain high-speed operation at 50 Gb/s, we formed p^- and n^- regions between high-doped regions and the center of the waveguide core, as shown in Fig. 1(b). We denote the doping levels of these p^- and n^- regions as N_A and N_D, respectively. We did not intentionally form these regions for 12.5-Gb/s and 25-Gb/s operation. Instead, long time annealing was applied to diffuse the dopants in the p^+ and n^+ regions into the waveguide core. We fabricated both PN and PIN diodes; the former had no gap between the p^- and n^- regions, whereas the latter had a gap of 440 nm, indicated as G

TABLE I
STRUCTURAL PARAMETERS AND PROCESS CONDITIONS OF FABRICATED MZMS

Sample notation	p^- and n^- dopant concentration (cm^{-3})	Doping type	G (nm)	Activation annealing	L (μm)
A	$N_A \approx 1\times10^{19}$, $N_D \approx 3\times10^{18}$	PN	0	10 s	100
B					250
C		PIN	440		250
D	$N_A \approx 3\times10^{18}$, $N_D \approx 1\times10^{18}$	PN	0		100
E					250
F		PIN	440		250
G	None	PIN	-	20 min. [a]	100

[a] In total. After waveguide is made, Phosphorus is first implanted followed by 15-min. annealing. Next, Boron is implanted followed by 5-min. annealing.

in Fig. 1(b). The structural parameters of the fabricated MZMs are summarized in Table I.

As indicated in Fig. 1(b), the width and height of the waveguide core were set to 460 and 220 nm, respectively. The width and length of the fins were about 80 nm and 2 μm, respectively. The pitch of the grating was designed to be 285 nm so that the detuning of the operating wavelength of 1550 nm from the Bragg wavelength became sufficiently large. The lengths of the phase shifters of the fabricated MZMs were 100 or 250 μm, which are denoted as L in Fig. 1(a).

We used an inverted taper as the optical coupling structure for all devices presented in this paper. At the facets of the samples, the width of the waveguides linearly decreases from 460 to 200 nm, from inside to the edge of the samples. The facets were polished to make them optically smooth after the samples were cut off from the wafer. In the measurements, we used lensed fibers and piezostages for the optical couplings and alignments.

B. Fabrication Process

The devices were fabricated in the super-clean-room at AIST Tsukuba West by using the process technology for CMOS devices. For the fabrication of the side-wall-grating waveguides, photolithography using the ArF immersion exposure system can be used to define the waveguide pattern. There have been few reports on fabrication using state-of-art photolithography [28], [29], such as ArF immersion exposure, and it has not been clarified if it is possible to fabricate such fine patterns as side-wall gratings. Fig. 2 shows a scanning electron microscopy (SEM) image of the fabricated passive waveguide with side-wall grating when we used the ArF immersion exposure system. It exhibited smooth and sharp edges of silicon, as shown in Fig. 2, which verifies the effectiveness of advanced photolithography for silicon photonics. So far, we have only fabricated passive side-wall-grating waveguides without doped regions or electrodes by using the ArF immersion exposure system. We are planning to fabricate the full MZM with doped regions and electrodes using the waveguide in Fig. 2, in the next step.

For the MZMs with doped regions and electrodes, we used a variable-shaped-beam electron-beam (VSB-EB) writer for defining the side-wall-grating waveguides in our current and previous works. We fabricated several MZMs (Samples A–G),

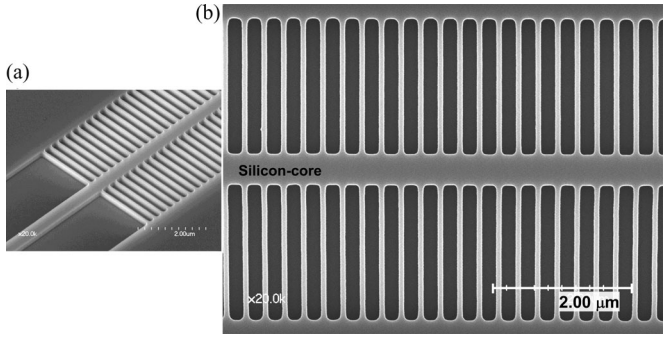

Fig. 2. SEM image of fabricated side-wall-grating waveguides before being covered with upper cladding layer. These waveguides are fabricated using ArF immersion exposure lithography.

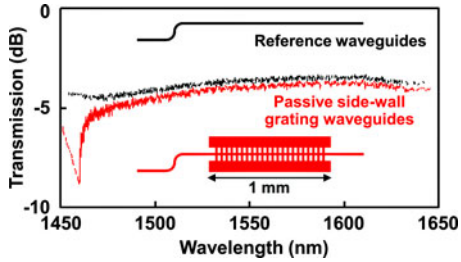

Fig. 3. Transmission spectrum of waveguides fabricated using ArF immersion exposure system. Red and black curves show spectrum of waveguides with and without side-wall gratings. Two and four samples were measured from identical chip, and all measured spectra are shown in the figure. Results were so uniform for both waveguide patterns that measured curves can hardly be distinguished.

which had different structures, as summarized in Table I. For MZMs with p^- and n^- regions (Samples A–F), dopants were implanted four times on a uniform SOI layer prior to forming waveguides, which resulted in p^+, n^+, p^-, and n^- regions. Phosphorus (P+) and boron (B+) were used for n- and p-type doping, respectively. After implantations, thermal activation was done for 10 s at 1000 °C followed by waveguide formation. For the MZM without p^- and n^- regions (Sample G), we used a different flow of processes, which was described in a previous paper [20]. A 1-μm-thick layer of silicon dioxide was deposited to cover the waveguide as a cladding layer. Finally, contact windows were opened on silicon pads, and 1-μm-thick aluminum was deposited to make contact.

C. Transmission Property of Side-Wall-Grating Waveguides

Fig. 3 is the measured transmission spectrum of passive waveguides with and without side-wall gratings. They were fabricated using photolithography of ArF immersion exposure. We measured two side-wall-grating waveguides and four reference waveguides without the gratings, which were all on the identical chip. All measured spectrum are shown in Fig. 3, by red and black curves, for side-wall-grating and reference waveguides, respectively. For each structure, the measured curves are very close to each other, and can hardly be distinguished. The average transmission in 1545–1555 nm was extracted from each curve. They were −3.58, −3.66, −3.61, and −3.59 dB for the four reference waveguides, and the standard deviation was only 0.04 dB. The four waveguides were put in a row within about

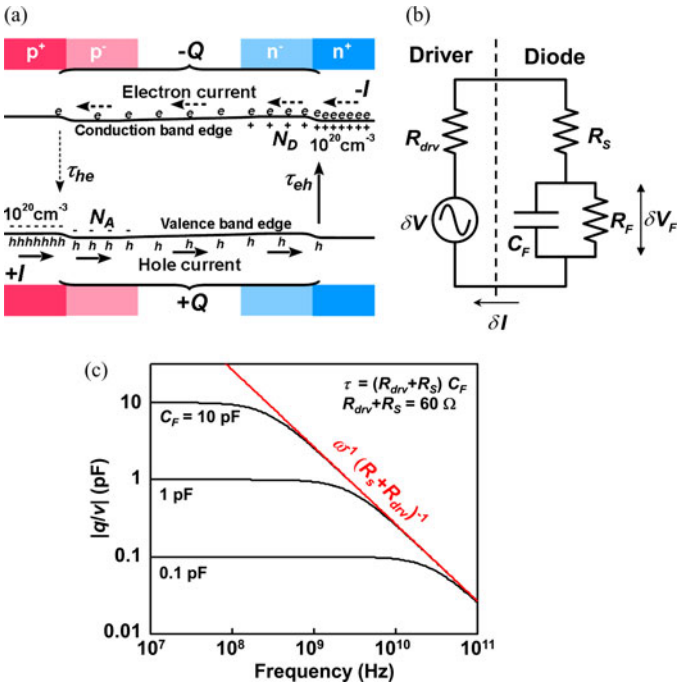

Fig. 4. Modeling and analysis of forward-biased PN-diode. (a) Energy band diagram of phase shifter. (b) Equivalent circuit of (a). (c) Frequency dependences of stored carrier q in capacitance C_F calculated using circuits of (b).

3-mm-wide area on the sample chip. The small deviation of transmission indicates the uniformity of the ArF immersion exposure, as well as small measurement error.

In Fig. 3, as the red lines indicate, the waveguides exhibited a stop-band due to the side-wall gratings around 1460 nm. At longer wavelengths than the stop-band, the spectrum exhibited a wide pass-band, which was as smooth and flat as the reference waveguides. We set the operating wavelength in this pass-band to around 1550 nm. The excess propagation loss of the side-wall-grating waveguides compared to the reference waveguide was only 0.4 dB/mm. This result indicates that the side-wall grating is useful as a basic waveguide structure for modulators and can be fabricated using CMOS standard processes.

III. Circuit Modeling of Forward-Biased Diode

In this section, we explain an equivalent circuit model, which was used to analyze the frequency response of our MZMs. Fig. 4(a) shows the physical model of the phase shifter in Fig. 1(b). We defined the carrier recombination times τ_{he}, and τ_{eh}, which mainly consist of Auger recombination [30] and surface recombination [31], [32]. The stored charge $Q(t)$ in the phase shifter satisfies the following rate equation:

$$\frac{dQ(t)}{dt} = I(t) - \left(\frac{1}{\tau_{he}} + \frac{1}{\tau_{eh}}\right) Q(t) \tag{1}$$

where $I(t)$ is the injected current flow into the phase shifter.

Fig. 4(b) shows the equivalent circuit of the forward-biased diodes for the phase shifter. This circuit is the same as the well known equivalent circuit for forward-biased diodes [10], and we can apply the same analysis as in our previous study [27]. Note that the modulator is electrically open without load resistance parallel to the modulator. This open-termination of the modulator does not degrade its frequency response because the length of the phase shifter was small enough, as shown in Table I. The diode dc current and the Q exhibit strong nonlinear dependence on the forward-bias voltage V_F. We use small signal analysis and introduce differential diode resistance R_F and the differential capacitance C_F

$$\delta Q(t) = C_F\, \delta V_F(t). \tag{2}$$

The relation of small values δI, δQ, and δV_F for the equivalent circuit is expressed as follows:

$$\delta I = \frac{d(\delta Q)}{dt} + \frac{\delta V_F}{R_F}. \tag{3}$$

From (1), (2), and (3), the carrier recombination times are expressed as

$$\frac{1}{\tau_{he}} + \frac{1}{\tau_{eh}} = \frac{1}{C_F R_F}. \tag{4}$$

The series resistance in Fig. 4(b) consists of both driver output impedance $R_{\rm drv} = 50\ \Omega$, and bulk resistance in the p- and n-doped regions R_s. When the system varies with time at frequency ω as $\delta Q(t) = q\ \mathrm{e}^{i\omega t}$ and $\delta\ V(t) = v\ \mathrm{e}^{i\omega t}$, we obtain q from (1)–(4) as follows:

$$q = \frac{C_F\, v}{1 + i\omega\tau}\left[\frac{\tau}{(R_{\rm drv} + R_s)C_F}\right] \tag{5}$$

where $\tau^{-1} = [(R_{\rm drv} + R_S)\ C_F]^{-1} + (R_F\ \mathrm{C}_F)^{-1}$. In (5), if $(R_{\rm drv} + R_S) \ll R_F, \tau \approx (R_{\rm drv} + R_S)\ C_F$. This means the recombination time does not so affect the behavior of the circuit. In Section IV-A, we discuss the parameters of the equivalent circuit of Fig. 4(b) deduced from the measured S-parameters. In fact, the results show that $(R_{\rm drv} + R_S) < R_F$ holds, as speculated in the previous study [27]. In general, (5) indicates that the response of the modulator is dominantly determined by the faster one between the circuit time constant $(R_{\rm drv} + R_S)C_F$ and the carrier recombination time $R_F\ \mathrm{C}_F$. In other words, we can increase the bandwidth of the modulator by reducing not only the recombination time [10] but also the circuit parameters, $R_{\rm drv} + R_S$.

To increase the bandwidth of the modulator, reducing $R_{\rm drv} + R_s$ is more meaningful than reducing the carrier recombination time. In forward-biased operation, the capacitance C_F is so large that the bandwidth of the modulator would not probably exceeds 10 GHz, even if using any of the two methods. In this case, the response of the modulator approaches $q/v \approx [i\omega\ (R_{\rm drv} + R_S)]^{-1}$, independently of the carrier recombination time $R_F\ \mathrm{C}_F$, at the operating frequencies, as derived from (5). This means that by reducing $R_{\rm drv} + R_s$, we can obtain the larger response $|q/v|$ of the modulator, as well as the higher bandwidth, whereas reducing the recombination time can only improve the bandwidth. In addition, if the bandwidth of the modulator cannot be large enough for higher speed operation at 20–50 Gb/s, preemphasis is necessary for forward-biased operation. Thus, the bandwidth of the modulator is less important for forward-biased operation compared with the absolute response $|q/v|$.

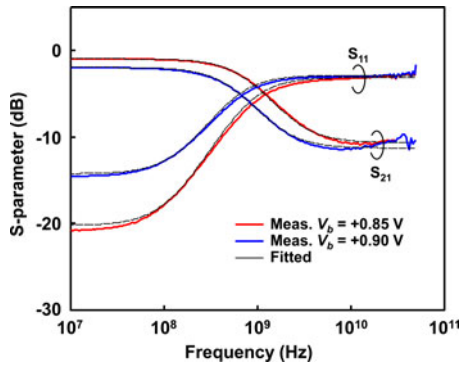

Fig. 5. Measured S-parameters of fabricated MZM (Sample C in Table II). Forward bias voltages were +0.85 V (red) and +0.90 V (blue). Black narrow lines are fitted curves obtained by circuit in Fig. 4(b) and parameters listed in Table I.

Fig. 4(c) shows the frequency response of $|q/v|$ calculated from (5), where $|q/v|$ expresses the efficiency of the modulator since the phase shift is largely proportional to the amount of stored charge. In the calculation, we set $\tau = (R_{\rm drv} + R_S)\, C_F$ and $R_{\rm drv} + R_S = 60\,\Omega$. In the figure, three curves with different values of C_F approach the single red line of $[\omega(R_{\rm drv} + R_S)]^{-1}$, regardless of the choice of C_F. This means the capability of the circuit to store the charges in the modulator is determined by $R_{\rm drv} + R_S$. For relatively small frequencies, too small capacitance limits $|q/v|$; for example, $|q/v|$ with $C_F = 0.1$ pF is smaller than the other curves with large C_F at 10 GHz. In other words, the capacitance should be large enough to use the full capability of the driver circuit. When compact modulators are needed, the capacitance per unit length should be large to obtain a large enough total capacitance. Thus, we used the forward-biased operation of the diodes for the better modulation efficiency at small lengths of the phase shifter.

IV. Characteristics of MZMs

In this section, we describe the measured characteristics of our fabricated MZMs. The structures of the MZMs used in the experiments are summarized in Table I.

A. High-Frequency Response

First, we measured the electrical S-parameters of the MZMs. We used sample C, which was based-on PIN diodes with $G =$ 440 nm, at relatively high junction concentrations. We measured S_{11} reflection and S_{21} transmission of the electrode of one of the two phase shifters on this MZM. We set two electrical contacts on both sides of the phase shifter in traveling-wave configuration. Fig. 5 shows the measured S-parameters with forward-bias voltage of $V_b = 0.85$ and 0.90 V. Both S_{11} and S_{21} greatly change at a frequency around several-hundred megahertz, which corresponds to the cut-off frequency of the circuit in Fig. 4(b).

Assuming the circuit topology in Fig. 4(b), we fitted the measured S-parameters, as the black narrow curves show in the figure. The measured curves were reasonably reproduced by using the circuit parameters in Table II. As indicated, R_F is about three times larger than $R_{\rm drv} + R_S$. From Table II, the two kinds

TABLE II
Extracted Circuit Parameters

V_b[a] (V)	C_F (pF)	R_S (Ω)	R_F (Ω)
0.85	6.5	10.5	219
0.87	8.9[b]	10.0[b]	158[b]
0.90	11.5	9.5	93.5

Extracted from measured S-parameters of Sample C shown in Fig. 5. "V_b: bias voltage, [b]linear interpolation between 0.85 and 0.9 V.

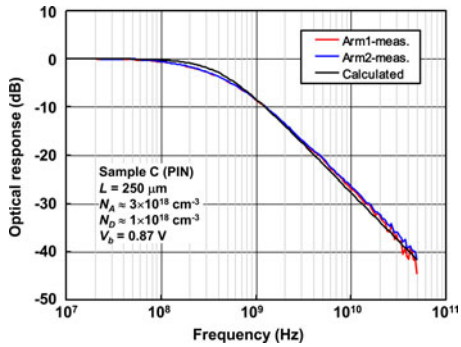

Fig. 6. Optical response of fabricated MZM (Sample C in Table I) with forward bias voltage of $V_b = 0.87$ V. Red and blue curves show results of two phase shifters on MZM, which were independently driven by small-amplitude signals. Black narrow lines are fitted curves obtained by circuit in Fig. 4(b) and parameters listed in Table II.

of time constant of the modulator is evaluated for $V_b = 0.87$ V; $(R_{\rm drv} + R_S)\, C_F = 534$ ps and $R_F\ C_F = 1.41$ ns. Thus, the circuit time constant determines the bandwidth of our modulator rather than carrier recombination time. If we reduce the recombination time to 100 ps by using the same means proposed by Zhou *et al.* [10], it would become smaller than $(R_{\rm drv} + R_S)\, C_F$ and we could obtain faster response of the modulator, too. However, as mentioned in the previous chapter, this means could not increase the response $|q/v|$ of the modulators.

Next, we examined optical responses for small modulation signals. We did not apply 50-Ω termination to the MZM and kept it electrically open, which was exactly the same configuration as in Fig. 4(b). Fig. 6 shows the measured response of the same MZM (Sample C). The measured curves are similar to those in Fig. 4(c). They exhibited a cut-off frequency of around several-hundred megahertz, and at higher frequencies, the curve declined by −20 dB/decade.

The black curve is the calculated response of $|q/v|$ using the circuit in Fig. 4(b) and the parameters listed in Table II. The measured curves were well fitted up to the highest frequency in the graph. These results indicate that equivalent circuit in Fig. 4(b) is valid for high-frequency operation of forward-biased PIN-diodes.

These results indicate that the forward-biased PIN diodes electrically behave as lumped elements, as modeled in Fig. 4. This is not the case if the distances between the doped regions and the core are too large. Fig. 7 shows the dependences of optical responses of forward-biased PIN diodes on the distance S in Fig. 1(b) [21]. For relatively small S, the slope of the response is about −20 dB/decade above the cut-off frequency, as expected from the lumped-RC circuit in Fig. 4(b). However, for relatively large S, the rate of decline above cut-off frequency became

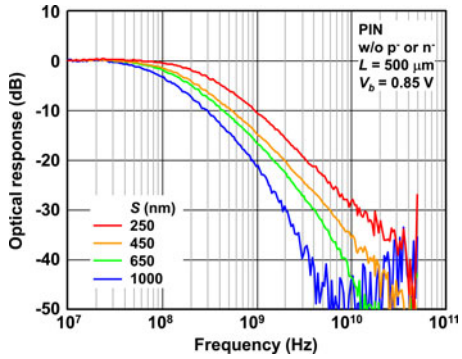

Fig. 7. Optical frequency response of our fabricated MZM with different values of S in Fig. 1(b) (colored lines) [21]. The samples had similar structure as Sample G in Table I. They did not have p- and n- regions, and instead the dopants in p+ and n+ regions were intentionally diffused to the waveguide core.

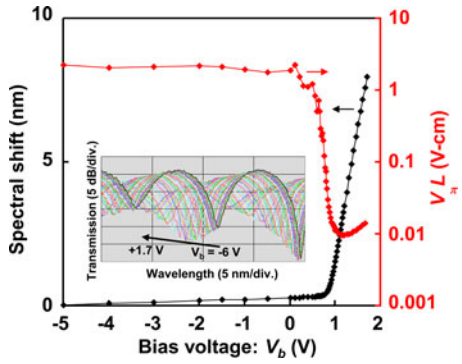

Fig. 8. Measured $V_\pi L$ as function of bias voltage of fabricated MZM (Sample C). Inset shows transmission spectrum of MZM with different bias voltage.

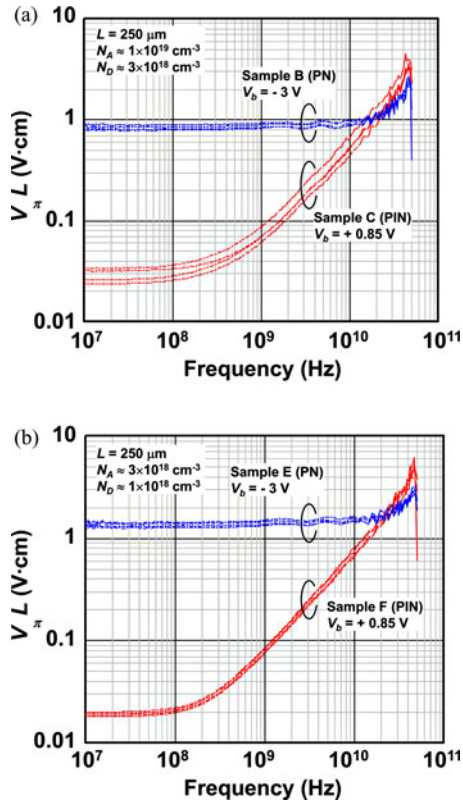

Fig. 9. Frequency dependences of $V_\pi L$ with different bias voltages. (a) For sample B (PN) and C (PIN) at relatively high concentration of p^- and n^- with $L = 250\ \mu$m. (b) For sample E (PN) and F (PIN) at relatively high concentration of p^- and n^- with $L = 250\ \mu$m. PN- and PIN-diodes are dc-biased at –3 and +0.85 V, respectively. Four diodes in two MZMs were measured for each device structure.

steeper than -20 dB/decade. In this case, a more complicated equivalent circuit would be needed. For 50-Gb/s devices, we used p^- and n^- regions in addition to decreasing S to avoid large optical loss due to free-carrier absorption in p^+ and n^+ doped regions.

B. Frequency-Dependent $V_\pi L$

$V_\pi L$, a product of the voltage and length of the phase shifter to obtain phase change of π, is a performance index often used to compare the efficiency of different kinds of modulators. Throughout this paper, $V_\pi L$ is of one of the two phase shifters in MZMs; it was calculated from the phase shift occurring at, voltage applied to, and length of only one of the two phase shifters. In forward-biased modulators, the measured $V_\pi L$ at dc is irrelevant for this purpose because the efficiency of those modulators strongly depends on frequency, as shown in previous studies [6], [8]–[12], [19]–[23] and in Fig. 6. We next normalized the optical response in Fig. 6 by $V_\pi L$ measured at dc to obtain frequency-dependent $V_\pi L$. Fig. 8 shows the measured dc-$V_\pi L$ as a function of the bias voltage. We measured the shift of the transmission spectrum of an asymmetric MZI, as shown in Fig. 1(a), by changing the applied bias voltages, as shown on the left axis in Fig. 8. The red line on right axis indicates the resultant $V_\pi L$. As expected, $V_\pi L$ at forward bias voltages exhibits about a 100-times reduction compared with that of reversed bias voltages.

Using these bias-voltage-dependent $V_\pi L$s and optical frequency responses, we obtained frequency-dependent $V_\pi L$ at different bias voltages, as shown in Fig. 9. This frequency-dependent $V_\pi L$ is valid for the 50-Ω driving circuit with $R_{\rm drv} = 50\ \Omega$ in Fig. 4(b). The phase change efficiency is defined for the amplitude of the δV in Fig. 4(b). We normalized response at the lowest frequency using the measured dc-$V_\pi L$. Though $V_\pi L$s have strong dependences at low frequencies on bias-voltages, they converge at high frequencies around 20 GHz. Below these frequencies, forward-biased operation exhibits smaller $V_\pi L$ than the reversed-biased operation.

With these results, the advantage of forward-bias operation may not be clear for high-speed operation at 50 Gb/s. However, the key point is that this converging frequency depends on the other parameters, such as the series resistance $R_{\rm drv} + R_s$ and the length of the phase shifter. Although we used $R_{\rm drv} = 50\ \Omega$ in the experiments in this paper, we do not have to adhere to this traditional load resistance. In particular, in aforementioned SOIPs, both photonic and electronic devices can be optimized for the better total performances. As mentioned in the previous chapter, by designing a driver circuit with low output impedance $R_{\rm drv}$, we could obtain more $|q/v|$ for forward-biased diodes, which have sufficiently large capacitance. By contrast,

TABLE III
PERFORMANCE SUMMARY OF FABRICATED MZMS

Sample notation	p^- and n^- dopant concentration (cm^{-3})	Doping type	L (μm)	Propagation loss (dB/mm)	$V_\pi L$ (V-cm)					
					V_b = +0.85 V			V_b = -3.0 V		
					DC	10 GHz	20 GHz	DC	10 GHz	20 GHz
A	$N_A \approx 1\times10^{19}$, $N_D \approx 3\times10^{18}$	PN	100	18.9	0.025	0.32	0.61	0.84	0.90	0.98
B			250		0.030	0.52	1.00	0.83	0.94	1.11
C		PIN	250	12.8	0.029	0.53	1.05	N/A		
D	$N_A \approx 3\times10^{18}$, $N_D \approx 1\times10^{18}$	PN	100	7.6	0.022	0.47	0.90	1.43	1.55	1.61
E			250		0.023	0.77	1.48	1.36	1.52	1.66
F		PIN	250	4.8	0.019	0.73	1.45	N/A		

for reverse-biased diodes, the small capacitance limits the total stored charge and the reduction of $R_{\rm drv}$ would not work.

We measured frequency dependent $V_\pi L$s of MZMs with different structures and operating conditions, and extracted $V_\pi L$ at 10 and 20 GHz. The results are summarized in Table III. From the results of PN-diodes with $W = 0$ (samples A, B, D, and E), we found that forward-biased operation generally provides smaller $V_\pi L$ at any frequency, N_p and N_n, and L. As mentioned earlier, the differences are larger for smaller frequencies. Forward-bias operation of a 100-μm long phase shifter exhibited smaller $V_\pi L$ than that of a 250-μm phase shifter, whereas those for reversed-bias operation were almost the same. In other words, for a 100-μm long phase shifter, forward-biased operation exhibits smaller $V_\pi L$ than the reversed one, even at high frequency of 20 GHz, whereas the difference is small for a 250-μm phase shifter. These dependences can be explained based on the equivalent circuit analysis in the previous chapter, as follows.

For forward-biased operation, both 100-μm and 250-μm phase shifters exhibited sufficiently large capacitance for the capability of the driving circuit. The driver output impedance dominantly determines the amount of total stored charge in all diodes. Therefore, the decrease in L results in a minor impact on the total modulation depth, i.e., phase change of the modulator. This in turn causes an increase in modulation efficiency per unit length for a shorter phase shifter. For reverse-biased operation, the capacitances are not so large that they determine the amount of stored charge in the capacitance even at a high frequency of 20 GHz. Therefore, a decrease in L leads to a decrease in phase shift for a given driving voltage; thus, $V_\pi L$ does not change. It is worth mentioning that this advantage of forward-bias operation of relatively small phase shifters makes them suitable for use in resonator-based modulators, such as microring resonators, as well as compact MZMs. Usually, phase shifters shorter than 100-μm are used in such modulators. In fact, we recently have demonstrated efficient 50-Gb/s operation of ring-resonator-based modulator using forward-biased diodes [23].

For forward-biased operation of 250-μm long phase shifters, the $V_\pi L$s at forward-bias voltage are almost the same between PN and PIN diodes, whereas the latter exhibit smaller measured propagation loss. PN diodes exhibit more propagation loss due to larger free-carrier absorption. Finally, devices with larger N_p and N_n (A–C) indicate smaller $V_\pi L$ than those with smaller N_p and N_n (D–F), irrespective of the other parameters, at the expense of large propagation loss.

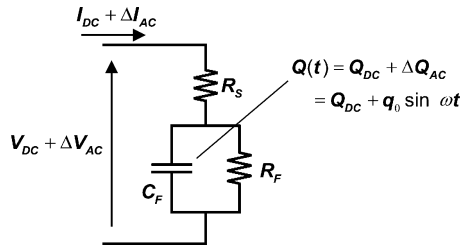

Fig. 10. Configuration and parameter assignment of modulator used in calculation of power dissipation.

C. Power Dissipation

Power consumption is another important metrics for the modulators. We evaluated the power consumption of the modulators in forward-biased operation by using the equivalent circuit in Fig. 4(b). For sake of simplicity, we calculated the power dissipation inside the modulator when it is operated by sinusoidal signals. By using the notation in Fig. 10, the average power dissipation P is expressed as follows:

$$\begin{aligned}\bar{P} &= \overline{(I_{\rm DC} + \Delta I_{\rm AC})\,(V_{\rm DC} + \Delta V_{\rm AC})} \\ &= I_{\rm DC}\,V_{\rm DC} + \overline{\Delta I_{\rm AC}\,\Delta V_{\rm AC}} \end{aligned} \tag{6}$$

where overline means taking average in time.

We assume the charges $Q_F(t)$ inside the capacitance of the diode C_F varies with time t such that $Q_F(t) = Q_{\rm DC} + \Delta Q_{\rm AC} = Q_{\rm DC} + q_0\ \sin(\omega t)$. As mentioned in the previous chapter, the amount of $\Delta Q_{\rm AC}$ determines the modulation depth via the FCP effect. From the equivalent circuit, both $\Delta I_{\rm AC}$ and $\Delta V_{\rm AC}$ are expressed by $\Delta Q_{\rm AC}$ as follows,

$$\begin{aligned}\Delta I_{\rm AC} &= \frac{{\rm d}\,(\Delta Q_{\rm AC})}{{\rm d}t} + \frac{\Delta Q_{\rm AC}}{R_F C_F}, \quad \text{and} \\ \Delta V_{\rm AC} &= R_s \frac{{\rm d}\,(\Delta Q_{\rm AC})}{{\rm d}t} + \frac{R_s}{C_F}\left(\frac{1}{R_S} + \frac{1}{R_F}\right)\Delta Q_{\rm AC}. \end{aligned} \tag{7}$$

By substituting, the aforementioned formula into (6), we obtain the power dissipation inside modulator for charge variation $\Delta Q_{\rm AC} = q_0\ \sin(\omega t)$, as follows:

$$\begin{aligned}\bar{P} &= I_{\rm DC}\,V_{\rm DC} + \overline{R_s\left[\frac{{\rm d}\,(\Delta Q_{\rm AC})}{{\rm d}t}\right]^2 + (R_s + R_F)\left(\frac{\Delta Q_{\rm AC}}{R_F C_F}\right)^2} \\ &= I_{\rm DC}\,V_{\rm DC} + \frac{R_s}{2}\,(\omega\,q_0)^2 + \frac{R_s + R_F}{2}\left(\frac{q_0}{R_F C_F}\right)^2. \end{aligned} \tag{8}$$

In the aforementioned formula, we dropped the products of $\Delta Q_{\rm AC}$ and its derivative because they are cyclic function and averaged out. In the rightmost formula in (8), the second term $R_s(\omega\ q_0)^2/2$ is essential for the operation of the modulator. When the charge in C_F is modulated with amplitude q_0, ac current of ωq_0 flows through R_s and causes inevitable power dissipation. Given that the required charge variation and the series resistance R_s are largely same between forward- and reveres-biased modes, this second term is roughly constant. The first and third terms in (8) represent dc and ac power dissipation, respectively, due to the leak current of the diode. Therefore, these are supposed to become larger for forward-biased operation than for reversed mode.

We can evaluate the power consumption by assigning values, which are obtained from the experiments, into (8). As described in the next chapter, $I_{\rm DC} = 0.36$ mA and $V_{\rm DC} = 0.5$ V, when sample C was operated at 50 Gb/s. Therefore, the first term in (8) is as small as 0.18 mW for one of the two phase shifters in the MZI. To determine the second and third term in (8), we used the values of *Rs*, R_F, and C_F, which are listed for sample C in Table II for $V_b = 0.87$ V. As for q_0, we calculated the required q_0 to obtain reasonable extinction ratio from the measured $V_\pi L$ of sample C; we assigned 0.51 pC to q_0. We used 25 GHz for the frequency, which corresponds to 50-Gb/s operation. With all these parameters the second and third term in (8) was equals to 32.4 and 0.011 mW, respectively, for one of the two phase shifters. These results indicate that the second term in (8), $R_s(\omega\ q_0)^2/2$, is dominant in the power dissipation of the FCP-based modulators. Thus, the leak currents give only negligible impact on the power dissipation of the forward-biased operation of the diode, and the intrinsic power dissipations are largely same between forward- and reverse-biased operations of the FCP-based modulators.

V. Large Signal Operation

Finally, we conducted large-signal modulation of the fabricated MZMs at 12.5 and 50 Gb/s. As mentioned earlier, our modulators are for SOIP applications, where a compact array of modulators is required. Fig. 11(a) shows a photograph of the modulator array fabricated for this purpose. The size of the modulator cell and the length of the phase shifter were as small as 50 μm $\times$ 300 μm and 100 μm, respectively. The modulator was designed for relatively low speed of up to 20 Gb/s, and did not have p^- and n^- regions. Instead, we intentionally diffused the dopants in the p^+ and n^+ regions into the adjacent part of the waveguide core by long-time high-temperature annealing [20]. We used preemphasis signals to drive the modulators, which were generated from conventional non-return-zero (NRZ) signals using inline differentiator. The preemphasis signals were amplified and leveled using a bias tee. We slightly adjusted the bias voltages around +0.95 V to keep the phase balance of the MZI at the quadrature point. The signals of 3.8–4.0 volt-peak-to-peak ($V_{\rm pp}$) were applied to the electrode of both phase shifters of the MZMs. Fig. 11(b) shows the measured optical eye diagrams of two of the four channels of the array at 12.5 Gb/s. We obtained clear eye openings with a dynamic extinction ratio

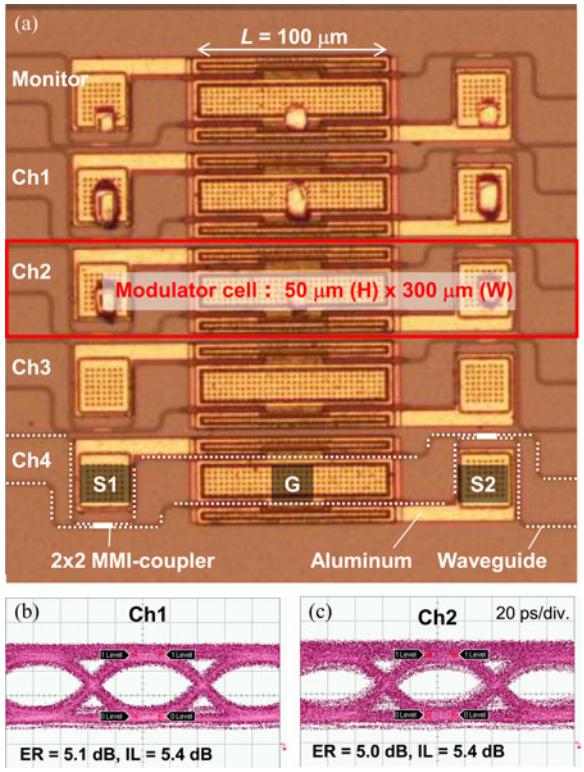

Fig. 11. (a) Four-channel compact modulator array. Each MZM has same structure as Sample G. (b) and (c) 12.5-Gb/s optical eye diagrams of two channels of modulator array. Waveforms were detected from one of two optical output ports of each channel. We confirmed that ER and IL from another output port were almost same as indicated in graphs.

(ER) of 5 dB. Only a single channel of the array was operated at once due to the limited configuration of the experiments. As indicated in Fig. 11(b) and (c), optical insertion loss (IL) was 5.4 dB for both channels. This IL includes all kinds of excess losses of MZMs during 12.5-Gb/s operation from the reference waveguide without the MMI coupler, side-wall-grating waveguides, or phase shifters. This IL includes 3-dB loss due to the power distribution between two output ports. The intrinsic loss of MZMs is only 2.4 dB (= 5.4 – 3.0).

For 50-Gb/s operation, we used sample C in Table I, which had a 250-μm long PIN-diode phase shifter with relatively high doping concentration [22]. Fig. 12(a) shows the experimental setup. We formed preemphasis signals from the NRZ signals by using in-line RF components, such as combiner and attenuators. This method is equivalent to using an FIR digital filter. The preemphasis signal was divided into two identical signals to drive the MZM in a push–pull configuration. Each of the two signals was amplified and leveled at +0.5 V for the forward-bias operation. Fig. 12(b) shows the resultant electrical waveform applied to each of the two arms of the MZM with 4.35 $V_{\rm pp}$. This amplitude was measured in an oscilloscope with system impedance of 50 Ω, though we left the electrodes of the MZM electrically open during the high-speed operation of the MZM. We kept the phase difference between the two arms at the quadrature during high-speed operation.

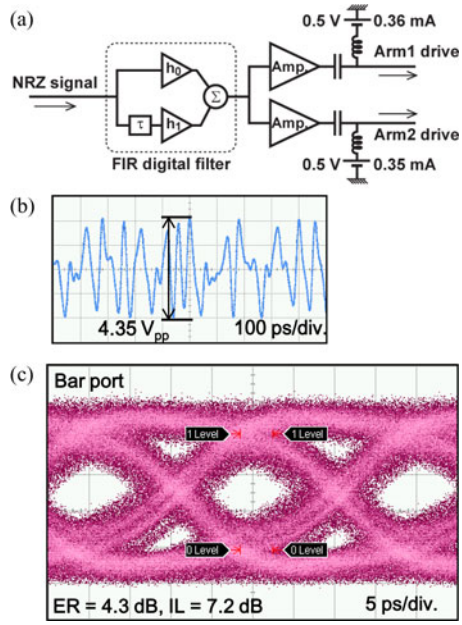

Fig. 12. 50-Gb/s-large signal modulation experiment using fabricated MZM (Sample C) [17]. (a) Setup to create preemphasis signals from standard NRZ signals in PRBS pattern of 2^7–1 using FIR digital filter. Preemphasis signals were divided into two identical electrical signals to drive MZM in push–pull configuration. (b) One of two electrical waveforms applied to modulator as output from bias tee in (a). (c) Optical 50-Gb/s eye diagrams obtained from bar ports of MZM. We also obtained about same ER from cross port.

Fig. 12(c) shows the optical output waveforms obtained from one of the two output ports (bar port) of the MZM. We successfully obtained eye openings at 50 Gb/s with dynamic ER of 4.3 dB. The measured IL was 7.2 dB, which was defined in the same manner as in 12.5-Gb/s operation. The ER and IL from the cross port was 4.1 dB and 7.0 dB, respectively. Both ER and IL are almost identical between the two ports, which confirm that the phase balance was kept at quadrature during the operation. The intrinsic loss of MZMs is 4.1 dB at this 50-Gb/s operation.

We next estimated the electrical power dissipated in the MZM during 50-Gb/s operation. During the operation, dc forward bias voltage of 0.5 V was applied to both diodes of two arms of the MZI. The measured dc currents were 0.36 and 0.35 mA, respectively. Then, dc power consumption P_{DC} was equal to about 0.36 mW. The ac power consumption P_{AC} can be estimated from the input voltage waveform $V(t)$ in Fig. 12(b). The P_{AC} is given by a time integral as

$$P_{\mathrm{AC}} = \frac{2}{T} \cdot \int_0^T \frac{\{V(t)\}^2}{R} dt. \tag{9}$$

in which T is the time span of the measured waveform. We used sufficiently long waveform with $T = 5$ ns. In (9), the factor 2 is needed because we used two identical signals to drive our MZM in push–pull configuration. We used 50 Ω as R since $V(t)$ was measured in 50 Ω systems, and then P_{AC} was estimated as 45 mW under an impedance matching condition. The estimated value must be larger than the dissipation power inside the MZM, because the MZM's impedance during high-speed operation was different from 50 Ω.

VI. Conclusion

We developed silicon MZMs that have side-wall-grating waveguides in the phase shifter sections for SOIP applications. The structure is easy to fabricate in terms of repeatability of the etching process of waveguides because no thin slab layer has to remain. We obtained a scattering loss of less than 0.4 dB/mm using waveguides fabricated by ArF immersion exposure.

We investigated the forward-biased operation of PIN-diodes using the equivalent circuit formed from the measured S-parameters. We argued that carrier recombination time only plays a minor role in that circuit. The impacts of the other critical parameters, such as driver output impedance and the length of the phase shifter, on the overall performance were discussed. In particular, reducing the driver output impedance is more important, which can increase the response of the modulator at high frequencies, as well as the bandwidth. Due to its large capacitance per length, the forward-biased operation provides efficient modulation for relatively short phase shifters. We found, by measuring frequency-dependent $V_\pi L$ of the fabricated MZMs, that forward-biased operation can provide higher efficiency than reversed ones even at high frequency of 20 GHz for 100-μm long phase shifters.

These results make those modulators suitable for the applications such as SOIPs, where low-driving voltage and compactness of the phase shifter are simultaneously required. We demonstrated efficient and high-speed operation of MZMs up to 50 Gb/s with forward-biased diodes by using a phase shifter as short as 100–250 μm and preemphasis signals. We showed 12.5-Gb/s operation of a compact silicon MZM array; each modulator cell was as small as 50 μm $\times$ 300 μm, including metal pads. The resulting driving voltages in those experiments were high for CMOS driver circuits. However, it is expected from our analysis that the voltage will be reduced for the forward-biased operation by using low-output-impedance driver, without increasing the length of the phase shifters. Furthermore, employing a ring-resonator is one of the promising approaches to reduce power consumption of SOIPs. For ring-resonator-based modulators, a short but efficient phase shifter is needed to reduce the driving voltage. Forward-biased diodes are suitable for such modulators, too [23].

References

[1] I. A. Young, E. M. Mohammed, J. T. S. Liao, A. M. Kem, S. Palermo, B. A. Block, M. R. Reshotko, and P. L. D. Chang, "Optical technology for energy efficient I/O in high performance computing," *IEEE Commun. Mag.*, vol. 48, no. 10, pp. 184–191, Oct. 2010.

[2] F. E. Doany, C. L. Schow, B. G. Lee, R. A. Budd, C. W. Baks, C. K. Tsang, J. U. Knickerbocker, R. Dangel, B. Chan, H. Lin, C. Carver, J. Huang, J. Berry, D. Bajkowski, F. Libsch, and J. A. Kash, "Terabit/s-class optical PCB links incorporating 360-Gb/s bidirectional 850 nm parallel optical transceivers," *J. Lightw. Technol.*, vol. 30, no. 4, pp. 560–571, Feb. 2012.

[3] X. Zheng, F. Y. Liu, J. Lexau, D. Patil, G. Li, Y. Luo, H. D. Thacker, I. Shubin, J. Yao, K. Raj, R. Ho, J. E. Cunningham, and A. V. Krishnamoorthy, "Ultralow power 80 Gb/s arrayed CMOS silicon photonic transceivers for WDM optical links," *J. Lightw. Technol.*, vol. 30, no. 4, pp. 641–650, Feb. 15, 2012.

[4] G. Kim, J. W. Park, I. G. Kim, S. Kim, S. Kim, J. M. Lee, G. S. Park, J. Joo, K.-S. Jang, J. H. Oh, S. A. Kim, J. H. Kim, J. Y. Lee, J. M. Park, D.-W. Kim, D.-K. Jeong, M.-S. Hwang, J.-K. Kim, K.-S. Park, H.-K. Chi, H.-C. Kim, D.-W. Kim, and M. H. Cho, "Low-voltage high-performance

silicon photonic devices and photonic integrated circuits operating up to 30 Gb/s," *Opt. Exp.*, vol. 19, no. 27, pp. 26936–26947, 2012.

[5] Y. Urino, Y. Noguchi, M. Noguchi, M. Imai, M. Yamagishi, S. Saitou, N. Hirayama, M. Takahashi, H. Takahashi, E. Saito, M. Okano, T. Shimizu, N. Hatori, M. Ishizaka, T. Yamamoto, T. Baba, T. Akagawa, S. Akiyama, T. Usuki, D. Okamoto, M. Miura, J. Fujikata, D. Shimura, H. Okayama, H. Yaegashi, T. Tsuchizawa, K. Yamada, M. Mori, T. Horikawa, T. Nakamura, and Y. Arakawa, "Demonstration of 12.5-Gbps optical interconnects integrated with lasers, optical splitters, optical modulators and photodetectors on a single silicon substrate," *Opt. Exp.*, vol. 20, no. 26, pp. B256–B263, 2012.

[6] G. T. Reed, G. Mashanovich, F. Y. Gardes, and D. J. Thomson, "Silicon optical modulators," *Nat. Photon.*, vol. 4, no. 8, pp. 518–526, 2010.

[7] A. Liu, R. Jones, L. Liao, D. Samara-Rubio, D. Rubin, O. Cohen, R. Nicolaescu, and M. Paniccia, "A high-speed silicon optical modulator based on a metal-oxide-semiconductor capacitor," *Nature*, vol. 427, pp. 615–618, 2004.

[8] Q. Xu, S. Manipatruni, B. Schmidt, J. Shakya, and M. Lipson, "12.5 Gb/s carrier-injection-based silicon micro-ring silicon modulators," *Opt. Exp.*, vol. 15, no. 2, pp. 430–436, 2007.

[9] W. M. J. Green, M. J. Rooks, L. Sekaric, and Y. A. Vlasov, "Ultra-compact, low RF power, 10 Gb/s silicon Mach-Zehnder modulator," *Opt. Exp.*, vol. 15, pp. 17106–17113, Dec. 2007.

[10] G.-R. Zhou, M. W. Geis, S. J. Spector, F. Gan, M. E. Grein, R. T. Schulein, J. S. Orcutt, J. U. Yoon, D. M. Lennon, T. M. Lyszczarz, E. P. Ippen, and F. X. Kärtner, "Effect of carrier lifetime on forward-biased silicon Mach-Zehnder modulators," *Opt. Exp.*, vol. 16, no. 8, pp. 5218–5226, 2008.

[11] S. J. Spector, M. W. Geis, M. E. Grein, R. T. Schulein, J. U. Yoon, D. M. Lennon, F. Gan, G.-R. Zhou, F. X. Kaertner, and T. M. Lyszczarc, "High-speed silicon electro-optical modulator that can be operated in carrier depletion or carrier injection mode," in *Proc. CLEO*, May 2008, pp. 1–2.

[12] S. J. Spector, C. M. Sorace, M. W. Geis, M. E. Grein, J. U. Yoon, T. M. Lyszczarz, E. P. Ippen, and F. X. Kartner, "Operation and optimization of silicon-diode-based optical modulators," *IEEE J. Sel. Topics Quantum Electron.*, vol. 16, no. 1, pp. 165–172, Jan./Feb. 2010.

[13] M. R. Watts, W. A. Zortman, D. C. Trotter, R. W. Young, and A. L. Lentine, "Low-voltage, compact, depletion-mode, silicon Mach–Zehnder modulator," *IEEE J. Sel. Topics Quantum Electron.*, vol. 16, no. 1, pp. 159–164, Jan./Feb. 2010.

[14] D. J. Thomson, F. Y. Gardes, Y. Hu, G. Mashanovich, M. Fournier, P. Grosse, J.-M. Fedeli, and G. T. Reed, "High contrast 40 Gb/s optical modulation in silicon," *Opt. Exp.*, vol. 19, no. 12, pp. 11507–11516, 2011.

[15] D. J. Thomson, F. Y. Gardes, J.-M. Fedeli, S. Zlatanovic, Y. Hu, B. P. P. Kuo, E. Myslivets, N. Alic, S. Radic, G. Z. Mashanovich, and G. T. Reed, "50 Gb/s silicon optical modulator," *IEEE Photon. Technol. Lett.*, vol. 24, no. 4, pp. 234–236, Feb. 15, 2012.

[16] T. Baehr-Jones, R. Ding, Y. Liu, A. Ayazi, T. Pinguet, N. C. Harris, M. Streshinsky, P. Lee, Y. Zhang, A. E.-J. Lim, T.-Y. Liow, S. H.-G. Teo, G.-Q. Lo, and M. Hochberg, "Ultralow drive voltage silicon traveling-wave modulator," *Opt. Exp.*, vol. 20, no. 11, pp. 12014–12020, May 2012.

[17] G. Li, X. Zheng, J. Yao, H. Thacker, I. Shubin, Y. Luo, K. Raj, J. E. Cunningham, and A. V. Krishnamoorthy, "High-efficiency 25 Gb/s CMOS ring modulator with integrated thermal tuning," presented at IEEE 8th Int. Conf. Group IV Photonics2011, London, U.K., Paper WA2.

[18] X. Xiao, X. Li, H. Xu, Y. Hu, K. Xiong, Z. Li, T. Chu, J. Yu, and Y. Yu, "44-Gb/s silicon microring modulators based on zigzag pn junctions," *IEEE Photon. Technol. Lett.*, vol. 24, no. 19, pp. 1712–1714, Oct. 1, 2012.

[19] J. Rosenberg, W. M. Green, A. Rylyakov, C. Schow, S. Assefa, B. G. Lee, C. Jahnes, and Y. Vlasov, "Ultra-low-voltage micro-ring modulator integrated with a CMOS feed-forward equalization driver," presented at Optical Fiber Communication Conf., Los Angeles, CA, USA, 2011, paper OWQ4.

[20] S. Akiyama, T. Baba, M. Imai, T. Akagawa, M. Takahashi, N. Hirayama, H. Takahashi, Y. Noguchi, H. Okayama, T. Horikawa, and T. Usuki, "12.5-Gb/s operation with 0.29 Vcm $V_{\pi}L$ using silicon Mach-Zehnder modulator based-on forward-bias pin diode," *Opt. Exp.*, vol. 20, no. 3, pp. 2911–2923, 2012.

[21] T. Baba, S. Akiyama, M. Imai, T. Akagawa, M. Takahashi, N. Hirayama, H. Takahashi, Y. Noguchi, H. Okayama, T. Horikawa, and T. Usuki, "25-Gbps operation of silicon p-i-n Mach-Zehnder optical modulator with 100-μm-long phase shifter," presented at the CLEO/IQEC (OSA), San Jose, CA, USA, 2012, Paper CF2L.3.

[22] S. Akiyama, T. Baba, M. Imai, T. Akagawa, M. Noguchi, E. Saito, Y. Noguchi, N. Hirayama, T. Horikawa, and T. Usuki, "50-Gbit/s silicon modulator using 250-μm-long phase shifter based on forward-biased pin diodes," presented at the IEEE 9th Int. Conf. Group IV Photonics, San Diego, CA, USA, 2012, Paper ThC2.

[23] T. Baba, S. Akiyama, M. Imai, N. Hirayama, H. Takahashi, Y. Noguchi, T. Horikawa, and T. Usuki, "50-Gb/s ring-resonator-based silicon modulator," *Opt. Exp.*, vol. 21, no. 10, pp. 11869–11876, 2013.

[24] C. Li, R. Bai, A. Shafik, E. Z. Tabasy, G. Tang, C. Ma, C.-H. Chen, Z. Peng, M. Fiorentino, P. Chiang, and S. Palermo, "A ring-resonator-based silicon photonics transceiver with bias-based wavelength stabilization and adaptive-power-sensitivity receiver," in *Proc. Int. Solid-State Circuits Conf.*, San Francisco, CA, USA, 2013, pp. 124–125.

[25] B. R. Moss, C. Sun, M. Georgas, J. Shainline, J. S. Orcutt, J. C. Leu, M. Wade, Y.-H. Chen, K. Nammari, X. Wang, H. Li, R. Ram, M. A. Popovic, and V. Stojanovic, "A 1.23 pJ/bit 2.5 Gb/s monolithically-integrated optical carrier-injection ring modulator and all-digital driver circuit in commercial 45 nm SOI," in *Proc. Int. Solid-State Circuits Conf.*, San Francisco, CA, USA, 2013, pp. 126–127.

[26] R. Soref and B. Bennett, "Electrooptical effects in silicon," *IEEE J. Quantum Electron.*, vol. QE-23, no. 1, pp. 123–129, Jan. 1987.

[27] T. Usuki, "Robust optical data transfer on silicon photonic chip," *J. Lightw. Technol.*, vol. 30, no. 18, pp. 2933–2940, Sep. 2012.

[28] S. K. Selvaraja, G. Murdoch, A. Milenin, C. Delvaux, P. Ong, S. Pathak, D. Vermeulen, G. Sterckx, G. Winroth, P. Verheyen, G. Lepage, W. Bogaerts, R. Baets, J. Van Campenhout, and P. Absil, "Advanced 300-mm waferscale patterning for silicon photonics devices with record low loss and phase errors," in *Proc.17th Opto-Electron. Commun. Conf.*, 2012, pp. 15–16.

[29] H. Takahashi, M. Toyama, M. Seki, D. Shimura, K. Koshino, N. Yokoyama, N. Ohtsuka, A. Sugiyama, E. Ishitsuka, T. Sano, and T. Horikawa, "The impacts of ArF excimer immersion lithography on integrated silicon photonics technology," presented at Int. Conf.on Solid State Devices and Materials (SSDM), Kyoto, Japan, Sep. 2012, paper A-2-1.

[30] M. J. Kerr and A. Cuevas, "General parameterization of auger recombination in crystalline silicon," *J. Appl. Phys.*, vol. 91, no. 4, pp. 2473–2480, Feb. 2002.

[31] P. P. Altermatt, J. O. Schumacher, A. Cuevas, M. J. Kerr, S. W. Glunz, R. R. King, G. Heiser, and A. Schenk, "Numerical modeling of highly doped Si:P emitters based on fermi-dirac statistics and self-consistent material parameters," *J. Appl. Phys.*, vol. 92, no. 6, pp. 3187–3197, Sep. 2002.

[32] B. Hoex, J. Schmidt, R. Boch, P. P. Altermatt, M. C. M. Van de Sanden, and W. M. M. Kessels, "Excellent passivation of highly doped p-type Si surfaces by the negative-charge-dielectric Al_2O_3," *Appl. Phys. Lett.*, vol. 91, no. 11, pp. 112107-1–112107-3, Sep. 2007.

Suguru Akiyama received the B.S. degree from the Tokyo Institute of Technology, Tokyo, Japan, in 1995, the M.E. degree from the University of Tokyo, Tokyo, in 1997 and the Ph. D. degree in engineering from Tsukuba University, Tsukuba, Japan, in 2013. In 1997, he joined Fujitsu Laboratories Ltd. Since then, he has been involved in semiconductor optoelectronic devices, in particular, high-speed modulators for optical fiber communications. He is currently a Chief Researcher at Photonics Electronics Technology Research Association (PETRA), Japan. Dr. Akiyama is a Member of the Japan Society of Applied Physics (JSAP) and the Institute of Electronics, Information and Communication Engineers (IEICE).

Masahiko Imai In 1986, he joined Fujitsu Laboratories Ltd. Since then, he has been involved in research and development of semiconductor process technologies. He is currently a Senior Researcher at Photonics Electronics Technology Research Association (PETRA).

Takeshi Baba In 2009, he joined Fujitsu Laboratories Ltd. He has been a Senior Researcher at Photonics Electronics Technology Research Association (PETRA) since 2010.

Takeshi Akagawa received the B.E. and M.E. degrees in applied physics from the Tokyo University of Agriculture and Technology, Tokyo, Japan, in 2003 and 2005, respectively. In 2005, he joined the System Devices Research Laboratories, NEC Corporation, Otsu, Japan, where he was involved in research and development on semiconductor lasers and optical modules. Since 2010, he has been with Photonics Electronics Technology Research Association, Tsukuba, Japan, where he is currently a Senior Researcher. Mr. Akagawa is a Member of the Japan Society of Applied Physics (JSAP) and the Institute of Electronics, Information and Communication Engineers (IEICE).

Naoki Hirayama, photograph and biography not available at the time of publication.

Yoshiji Noguchi received the B.S. degrees in chemical engineering from the Muroran Institute of Technology, Muroran, Japan, in 1985. He joined Texas Instruments Japan Limited in 1985, where he was involved in the process integration technology for VLSIs. In 2010, he moved to the Innovation Center for Advanced Nanodevices (ICAN), National Institute of Advanced Industrial Science and Technology (AIST), Tsukuba, Japan. He is now involved in the development of dry etching technology and process integration for PECST Project and Quantum Information Processing Project.

Miyoshi Seki joined NEC in 1992. He was also with Semiconductor Leading Edge Technologies, Inc., as a Lithography and Etching Engineer. He is currently the Advanced 300-mm CMOS ArF Immersion Lithography Process Engineer at the National Institute of Advanced Industrial Science and Technology and his current interests include cutting edge Silicon Photonics Lithography and Resist technology development.

Keiji Koshino, photograph and biography not available at the time of publication.

Munenori Toyama received the B.S. degree in electrical engineering from Miyazaki University, Miyazaki, Japan, in 1984. He was with SEIKO EPSON and Intel K.K. He is currently an Engineer of the Silicon Photonics Integration for the Advanced 300 mm CMOS process at the National institute of Advanced Industrial Science and Technology.

Tsuyoshi Horikawa received the B.S. degree and the M.S. degree in chemistry from Shizuoka University, Shizuoka, Japan in1983 and from Kyoto University, Kyoto, Japan in1985, respectively. He joined the Materials and Electronic Devices Laboratory, Mitsubishi Electric Corp., and then moved to the National Institute of Advanced Industrial Science and Technology (AIST), Tsukuba, Japan. He is currently the Deputy Director of the Innovation Center for Advanced Nanodevices (ICAN), AIST. His research interests include materials science and process technology in electronics and silicon photonics. He has been with PECST project since 2010. He is a Member of the IEEE Photonics Society and the Japan Society of Applied Physics.

Tatsuya Usuki received the B.S., M.S., and Ph.D. degrees from the Department of Applied Physics, Osaka University, Osaka, Japan, in 1986, 1988, and 1991. In 1991, he joined Fujitsu Laboratories Ltd., Atsugi, Japan, where he was involved in research on semiconductor physics and development of novel electron devices. From July 2005 to March 2009, he was an especially appointed Professor with the Institute of Industrial Science, the University of Tokyo, Tokyo, Japan. Since May 2010, he has been with Photonics Electronics Technology Research Association, Ibaraki, Japan, where he is currently a Chief Researcher.

Dr. Usuki is a Member of the Japan Society of Applied Physics, the IEEE Electron Device Society, and the American Physical Society.